

MonoDGP: Monocular 3D Object Detection with Decoupled-Query and Geometry-Error Priors

Fanqi Pu¹ Yifan Wang¹ Jiru Deng¹ Wenming Yang^{1*}

¹Shenzhen International Graduate School, Tsinghua University

{pfq23, yf-wang23, djr23}@mails.tsinghua.edu.cn, yang.wenming@sz.tsinghua.edu.cn

Abstract

Perspective projection has been extensively utilized in monocular 3D object detection methods. It introduces geometric priors from 2D bounding boxes and 3D object dimensions to reduce the uncertainty of depth estimation. However, due to errors originating from the object's visual surface, the bounding box height often fails to represent the actual central height, which undermines the effectiveness of geometric depth. Direct prediction for the projected height unavoidably results in a loss of 2D priors, while multi-depth prediction with complex branches does not fully leverage geometric depth. This paper presents a Transformer-based monocular 3D object detection method called MonoDGP, which adopts perspective-invariant geometry errors to modify the projection formula. We also try to systematically discuss and explain the mechanisms and efficacy behind geometry errors, which serve as a simple but effective alternative to multi-depth prediction. Additionally, MonoDGP decouples the depth-guided decoder and constructs a 2D decoder only dependent on visual features, providing 2D priors and initializing object queries without the disturbance of 3D detection. To further optimize and fine-tune input tokens of the transformer decoder, we also introduce a Region Segmentation Head (RSH) that generates enhanced features and segment embeddings. Our monocular method demonstrates state-of-the-art performance on the KITTI benchmark without extra data. Code is available at <https://github.com/PuFanqi23/MonoDGP>.

1. Introduction

3D object detection has always been a critical research topic in the fields of autonomous driving and robotic perception. Compared with LiDAR- [22, 46, 47, 59] or stereo-based [12, 23, 24, 40, 49] methods, monocular 3D object detection exhibits lower spatial positional accuracy without depth information. Owing to their cost-effectiveness and

*Corresponding author.

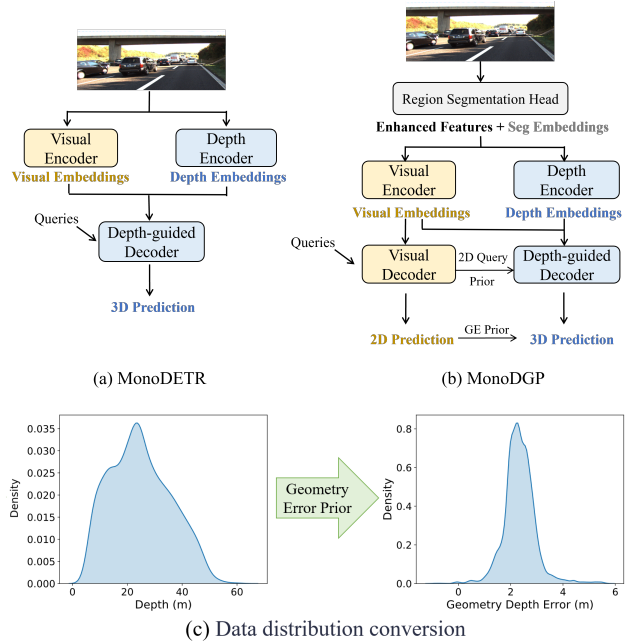


Figure 1. **Comparison with MonoDETR.** MonoDGP employs an RSH module for enhanced features and segment embeddings, along with an independent visual decoder for 2D query initialization. We further propose a geometry error prior that converts uneven depth distribution into more concentrated error distribution.

ease of configuration [26, 41], monocular methods have remained a primary focus of research in recent years.

Without extra data, the direct prediction of 3D objects from single 2D images is an extremely challenging problem. During the formation of 2D images, crucial depth-related information is compressed, resulting in an inherently ill-posed issue for direct depth estimation [26, 38, 42, 63, 66]. This limitation significantly undermines the accuracy of 3D object detection. However, under certain conditions, the uncertainty of depth estimation can be reduced with substantial prior knowledge. Particularly in the realm of autonomous driving, where the major objects of interest, such as cars, are rigid entities with known geometric properties.

Previous methods like Deep3DBox [36] and Shift R-

CNN [37] enforce geometric constraints through tight alignment between 3D box projections and 2D detections. Unlike strict constraints mentioned above, geometric depth is uniquely determined by the ratio of an object’s 3D height to its 2D projected height. This physically interpretable explicit mapping eliminates cascaded uncertainty, ensuring superior computational efficiency and noise robustness. However, since 2D images are inaccurate in capturing depth errors of the object visual surface, the 2D bounding box height often exceeds the projected height, which makes geometric depth deviate from the actual depth. To address single-depth prediction limitations, some approaches [26, 60, 62] integrate multi-depth predictions through weighted averaging, including direct and geometric depths. Nevertheless, MonoCD [60] indicates that if these predicted depths cluster on the same side of the ground truth depth, even weighted averaging fails to correct the depth error. DID-M3D [38] decomposes depth into visual and attribute parts, using perspective transformation for data augmentation. Similarly, the geometric depth can also be regarded as the visual depth, whose value depends on the object’s surface appearance and position [13]. While the depth error is determined by the object’s inherent attributes and remains invariant with changes in perspective. With more concentrated distribution, error prediction can not only alleviate the long-tail effect of raw depth, but also avoid the problem where multiple depths fail to complement each other after weighting.

After introducing the geometric prior, we observed that the accuracy of the bounding boxes is often poor during the initial training stage. This may lead the model to associate depth with incorrect bounding boxes, thereby complicating the convergence process. To address this issue, we decouple the depth-guided decoder proposed by MonoDETR [62] and construct a 2D visual decoder for independent 2D detection and query initialization. Additionally, we propose a Region Segmentation Head (RSH) to strengthen the foreground features and provide segment embeddings for semantically similar input tokens. By emulating BERT [19]’s approach to handling distinct components of textual inputs, we treat the target region as one “sentence” and the background region as another “sentence”.

In summary, we propose a transformer-based method called MonoDGP. Our contributions are listed as follows:

- We adopt perspective-invariant error prediction to replace multi-depth prediction, alleviating the long-tail effect of depth distribution and reducing learning complexities.
- We construct a decoupled visual decoder to initialize queries and reference points of the depth-guided decoder, boosting the model convergence and training stability.
- We present a Region Segmentation Head (RSH) to enhance object features and suppress background noise. Additionally, segment embeddings are incorporated dur-

ing depth encoding to refine contextual representations.

- Evaluated on the KITTI 3D object detection benchmark, without any extra data, MonoDGP achieves the state-of-the-art (SOTA) performance among monocular detectors.

2. Related work

Extra training data. The main challenge of monocular methods is insufficient of depth cues, which renders 3D object detection an ill-posed problem. Consequently, some approaches [17, 25, 38, 43, 54, 57] incorporate additional data, such as point clouds or depth maps, enabling the model to implicitly learn depth features during training. MonoPGC [57] introduces pixel-level depth map prediction as an auxiliary task, encoding 3D coordinates into depth-perception features to perceive the spatial positions of pixels. CaDDN [43] estimates the classified depth distribution for each pixel, generates high-quality bird’s-eye view feature representations, and achieves accurate 3D object predictions. OccupancyM3D [39] creates occupancy labels from point clouds, and monitors occupancy status in frustum space and 3D space. Given the reliance on expensive sensors and complex collection processes for supplementary information, MonoDGP exclusively utilizes monocular images during the training and inference stages, thereby enhancing the model’s practicality and deployment feasibility.

Transformer-based methods. Many previous works [26, 30, 33, 38, 48, 63] have employed convolutional neural networks (CNNs) to extract local, fine-grained information at various spatial levels. Although CNN-based methods demonstrate superior speed and efficiency, they require multi-layer convolution to progressively aggregate features for capturing long-distance dependencies. Additionally, non-maximum suppression (NMS) technology is employed to filter out redundant detection boxes. Benefiting from the global perception and dynamic adjustment abilities of the attention mechanism [53], an increasing number of studies [17, 62, 65] have shifted their focus toward Transformer-based monocular detectors. For instance, MonoDTR [17] proposes to conduct depth position encoding and integrates global depth information into the Transformer to guide the detection. MonoDETR [62] adheres to the DETR [8] architecture, utilizing object-level depth labels to predict the foreground depth map, constructing a depth-guided decoder, and incorporating object queries for global feature aggregation. MonoDGP also adopts the DETR framework, initializing queries with a decoupled 2D visual decoder and introducing segment embeddings to enhance the contextual relationships among pixels.

Multi-depth estimation modes. Early monocular methods [5, 11, 29, 31, 50] directly estimate object depth through end-to-end network training. Many researchers [1, 2, 7, 20, 48, 56, 64] extend the depth estimation branches

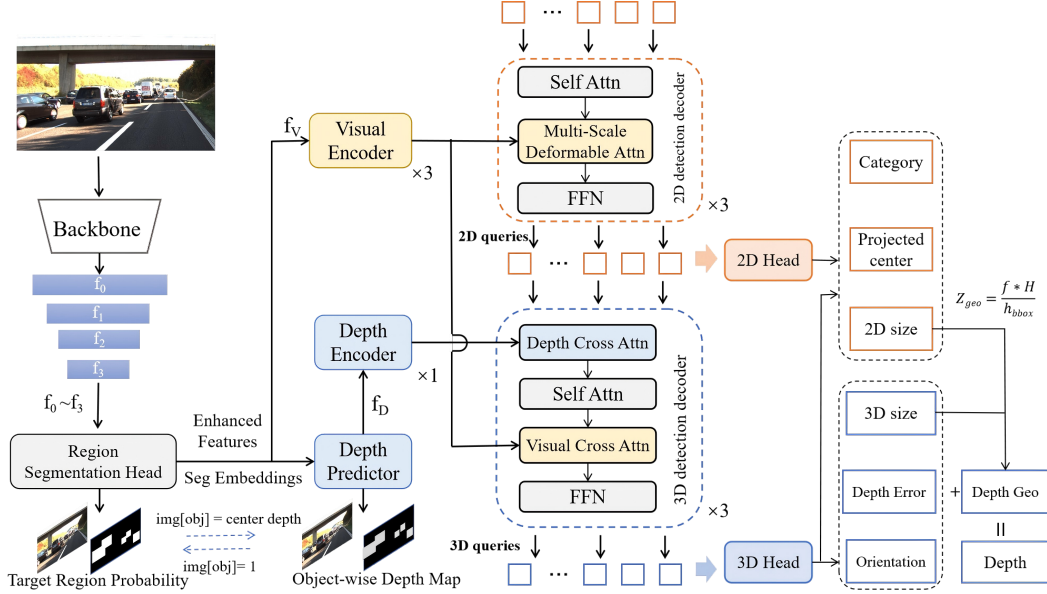


Figure 2. **Overall architecture of our MonoDGP.** The network comprises three components: feature extraction and enhancement, transformer encoder-decoder and object detection heads. The parallel visual and depth branches within the transformer are represented by yellow and blue, respectively. The predicted depth is separated into geometric depth Z_{geo} , obtained from the perspective projection formula, and depth error Z_{err} to correct the formula.

by introducing perspective projection and mathematical priors. For example, GUPNet [33] proposes a geometry uncertainty projection module and employs a Laplacian distribution to represent geometric depth with correlation-learned bias. To mitigate uncertainties in single depth estimation methods, MonoDDE [26] introduces key points into 20 different depth branches, emphasizing the significance of diversity in depth prediction. MonoDETR [62] merges predicted results from direct depth, object-level depth map, and geometric depth. MonoCD [60] further discusses the complementarity among multiple depths and combines them to cancel out positive or negative errors. However, the geometric depth and errors (such as depth/height error) in the projection formula have not been fully explored. Based on a comprehensive analysis of geometric priors, MonoDGP decouples raw depth to obtain perspective-invariant depth error, providing a superior alternative to multi-depth approaches.

3. Method

3.1. Overview

The overall framework of MonoDGP is shown in Fig. 2. Firstly, a single-view image is processed by ResNet50 to extract multi-scale feature maps $f_i \in \mathbb{R}^{\frac{H}{2^{i+3}} \times \frac{W}{2^{i+3}} \times C}$, $i = 0, 1, 2, 3$. The RSH module then predicts target region probabilities and enhances visual features f_V . A lightweight depth predictor subsequently estimates the depth map and

generates depth features f_D . Both enhanced visual features f_V and depth features f_D are fed into two parallel transformer encoders. The transformer decoder consists of a 2D visual decoder and a 3D depth-guided decoder. In the 2D decoder, object queries adaptively achieve semantic scene understanding from visual embeddings, while the 3D decoder extracts geometric and spatial relationships from both visual and depth embeddings. Ultimately, we utilize decoupled queries as inputs for 2D/3D detection heads separately. It is worth noting that after calculating geometric depth based on the projection formula, a geometry error correction mechanism is applied to improve the accuracy of depth estimation.

3.2. Region Segmentation

The Region Segmentation Head (RSH) is specifically designed to enhance the fine-grained foreground feature extraction. As shown in Fig. 3, the RSH follows the structure of U-Net [45] and predicts the target probability for each pixel. It is essential for the depth predictor to concentrate more on the perspective and geometric cues within the foreground area. Therefore, the RSH provides enhanced target features and segment embeddings for depth encoding. Technical details are presented below:

Region Segmentation and Enhancement. We initially utilize a ResNet backbone to downsample and extract multi-scale visual features f_0 to f_3 . Subsequently, We restore f_3 to high-resolution feature maps through upsampling opera-

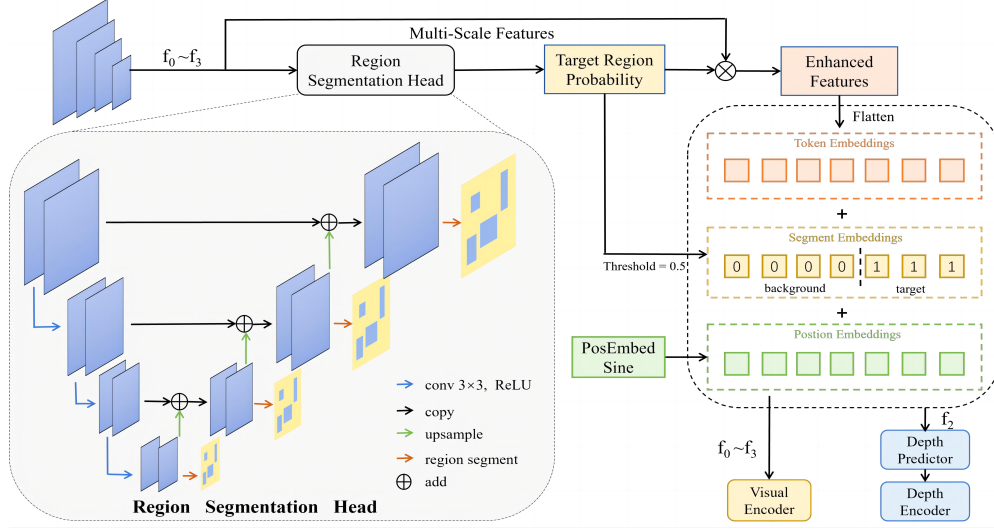


Figure 3. **The structure of region segmentation module.** The multi-scale feature maps are progressively upsampled and added, outputting target region probabilities by segment heads. Subsequently, enhanced features are achieved through element-wise multiplication with original features. Finally, segment embeddings are acquired under threshold constraints.

tions and skip connections. This integration of shallow and deep features improves multi-scale representation. Specifically, we combine the upsampled f_3 with f_2 after a 1×1 convolution and GroupNorm layer. This process is repeated to obtain fused feature maps at various scales. We then employ an SEBlock [16] for attention weighting on each scale’s feature maps. The SEBlock implements a channel attention mechanism through two 1×1 convolution layers: the first convolution reduces the number of feature channels to $1/16$, while the second convolution restores the original number of channels. Finally, we achieve several semantic segmentation maps with the sigmoid function. By multiplying the predicted target probability with original features, RSH effectively enhances foreground features and suppresses background noise.

Region loss. We construct target region masks and set the areas within bounding boxes to 1. Guided by these region masks, we calculate the Dice loss for the target region probabilities at each scale and weight the sum of these losses. The Dice loss, which is based on set similarity, addresses class imbalance and improves segmentation precision. Its definition is as follows:

$$L_{region}^i = 1 - \frac{2 \cdot \sum_{j=1}^{N_i} p_j \cdot g_j}{\sum_{j=1}^{N_i} p_j + \sum_{j=1}^{N_i} g_j} \quad (1)$$

Where p_j denotes the predicted probability of the j -th pixel, g_j represents the j -th pixel in the ground truth label, and N_i indicates the total number of pixels in the i -th feature map $f_i, i = 0, 1, 2, 3$. By minimizing the Dice loss, we can di-

rectly optimize the overlapping areas between the predicted probabilities and the region masks, enhancing both segmentation accuracy and consistency.

Segment embeddings. The RSH module generates segment embeddings from target region probabilities that exceed a threshold of 0.5. We subsequently add these segment embeddings to the token and position embeddings. This approach is inspired by the segment embeddings mechanism utilized in the BERT model [19]. Segment embeddings help to better distinguish the semantic relationships between foreground and background image tokens, similar to how different “sentences” are represented in BERT.

3.3. Decoupled Query

Geometric priors optimize depth estimation, but also introduce depth uncertainty to 2D detection. To mitigate this side effect, we decouple object queries for independent 2D detection. After obtaining visual embeddings f_V^e and depth embeddings f_D^e from two parallel encoders, MonoDGP decomposes the depth-guided decoder into a 2D decoder and a 3D decoder. The 2D visual decoder initialize 2D queries and reference points to acquire spatial position and category information. These 2D queries are then fed into the 3D decoder to interact with visual and depth features. This allows each decoder to focus on its own specific task and ensures stable convergence during training.

2D detection decoder. We take a set of learnable object queries $q \in \mathbb{R}^{N \times C}$ as input, which sequentially passes through an inter-query self-attention layer, a multi-scale deformable cross-attention layer [67], and a feedforward network(FFN), where N denotes the pre-defined maximum

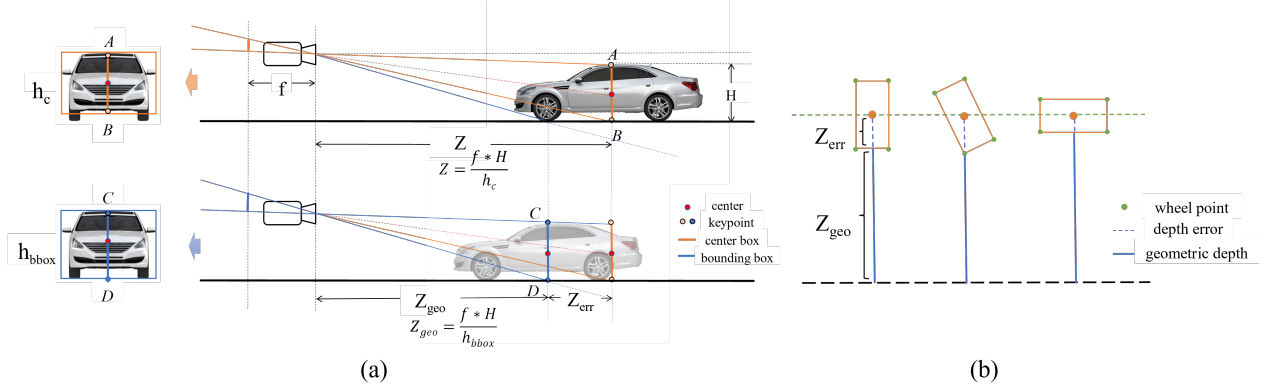


Figure 4. (a) **Schematic illustration of how geometry error occurs.** Due to the height of the bounding box h_{bbox} is larger than the projected central height h_c , there will be an error between geometric depth and ground truth depth. (b) **Vehicles at different angles in a bird's-eye view.** The geometric depth Z_{geo} is the distance between the camera plane and the parallel plane on which the closest wheel sits, while depth error Z_{err} only depends on the object's dimensions and orientation. The camera height also has a tiny effect on the Z_{err} , rigorous proof is given in the appendix.

number of objects in a single image. The 2D queries q_{2d} interact with visual embeddings f_V^e to extract 2D image features, including color, edges, and texture. The queries and reference points provide an initial perception of spatial positioning. The 3D decoder can utilize these 2D query priors to more rapidly focus on the target area in complex scenes.

3D detection decoder. The initialized 2D object queries $q_{2d} \in R^{N \times C}$ are input to the 3D depth-guided decoder. Each decoder block contains a depth cross-attention layer, an inter-query self-attention layer, a visual cross-attention layer and an FFN. Specifically, object queries first extract perspective cues from depth embeddings f_D^e . Subsequently, the depth-aware queries are sent to the inter-query self-attention layer to promote information exchange. After the visual cross-attention layer and FFN, we generate 3D queries q_{3d} that combine semantic and geometric features, obtaining an accurate scene-level spatial understanding.

3.4. Geometry Error

Direct depth estimation is often ill-posed in monocular methods. We apply the perspective projection formula $Z = f \times H_{3D}/h_{2D}$ to introduce geometric priors and mitigate depth uncertainty. When utilizing the projection formula, it is essential to make sure that the object's dimension height (such as AB and CD in Fig. 4(a)) is parallel to the projection plane, namely the X-Y plane in the camera coordinate system, and remains perpendicular to the X-Z plane. To guarantee the validity of the formula, we establish the following assumptions:

- The roll and pitch angles of the monocular camera are set to 0 degrees by default.
- The influence of ground slope can be overlooked when calculating geometric depth.

Under the given assumptions, the projected central

height h_c is solely dependent on the 3D height and depth, while the height of the 2D bounding box h_{bbox} can be influenced by additional factors, including its shape and surface characteristics. As illustrated in Fig. 4 (a), the visual disparity typically causes a depth error Z_{err} between the actual depth Z and the geometric depth Z_{geo} , which can be formulated as:

$$Z = \frac{f \cdot Y_{AB}}{v_{AB}} = \frac{f \cdot H}{h_c}, Z_{geo} = \frac{f \cdot Y_{CD}}{v_{CD}} = \frac{f \cdot H}{h_{bbox}} \quad (2)$$

$$Z = Z_{geo} + Z_{err} \quad (3)$$

where f denotes the focal length of the camera.

The Z_{geo} reflects the visible surface depth, while Z_{err} is only related to the inherent attributes of the object. In comparison to the raw depth Z , Z_{err} is perspective-invariant with less spatial uncertainty. We replace the direct depth prediction with the geometry error prediction, and our depth loss is calculated as follows:

$$L_{depth} = \frac{\sqrt{2}}{\sigma_d} \|Z_{geo} + Z_{err} - Z_{gt}\|_1 + \log(\sigma_d) \quad (4)$$

The perspective projection formula contains two variables: the height of the 2D bounding box and the height of the 3D size. To correct the formula, the depth error is added to the geometric depth for the final prediction, while errors from both the 2D and 3D heights can also compensate for the geometric depth. Their predictions are formulated as:

$$Z = \frac{f \cdot (H + H_{err})}{h_{bbox}} = Z_{geo} + \frac{f}{h_{bbox}} \cdot H_{err} \quad (5)$$

$$Z = \frac{f \cdot H}{h_c} = \frac{f \cdot H}{h_{bbox} - h_{err}} \quad (6)$$

These errors can significantly improve the performance of geometric depth.

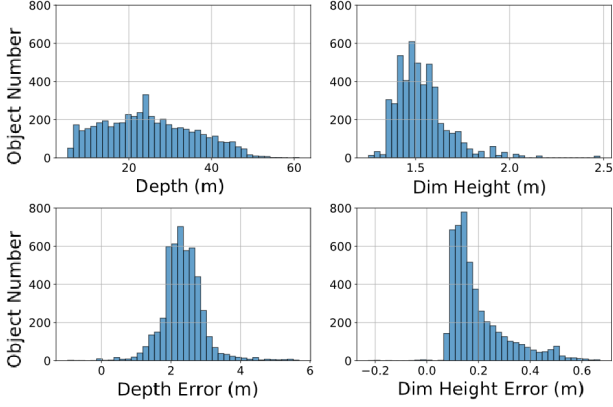


Figure 5. **Comparison of 3D data distributions.** With the total number of objects remaining constant, each distribution is visualized using a histogram.

3.5. Why Geometry Error Works?

The geometry error eliminates perspective correlation of raw depth distribution, thus reducing the learning difficulty of the network. Specifically, the reasons why geometry error works can be analyzed from three aspects:

- 2D and 3D attributes: why we utilize h_{bbox} instead of h_c in the projection formula?
- Different 3D attributes: why raw depth performs worse than other 3D attributes?
- Different geometry errors: why we select depth error?

2D and 3D attributes. 2D predictions rely on monocular visual features like color, edges, textures, whereas 3D predictions require extra factors including depth positioning and geometric perspective, which are difficult to obtain from single-view images. Benefiting from the network’s powerful capability of marginal feature extraction, h_{bbox} can provide more accurate 2D priors. However, we can hardly predict h_c from direct marginal features. The geometric depth calculated by h_{bbox} should be regarded as a reliable surface depth, rather than an inaccurate central depth.

Different 3D attributes. Without direct depth supervision, data distribution dictates network learning complexity. The Fig. 5 and 6 show the data distributions and boxplot of depth-related 3D attributes. Based on these figures, we can further evaluate and compare the learning difficulty across different data distributions. The central depth exhibits a long-tailed distribution with wide variance, while the 3D size distribution tends to be more concentrated. For instance, typical car height clusters near 1.5 meters, simplifying pattern recognition. The boxplot indicates that the depth distribution has a broader interquartile range (IQR) and longer whiskers, suggesting greater complexity and noise. Meanwhile, the IQR for dimension height, depth error,

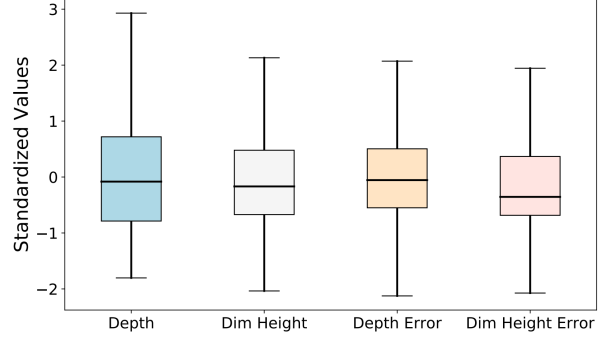


Figure 6. **The boxplot of depth-related attributes.** To conduct unified comparisons, the data distributions of different attributes are standardized by $X' = (X - \mu)/\sigma$ in the boxplot.

error, and height error is narrower, which illustrates that these distributions are relatively compact with plain patterns.

Different geometry errors. (1) Depth error Z_{err} and dimension height error H_{err} : Both Z_{err} and H_{err} have a narrow IQR and short whiskers, indicating that they share similar statistical properties. The primary distinction is that Z_{err} distribution is symmetrical with a median close to zero, while H_{err} distribution is skewed with a negative median. This skewness may increase the complexity of the training process. According to Eq. (3) and Eq. (5), we can express H_{err} in terms of Z_{err} and h_{bbox} :

$$H_{err} = \frac{1}{f} \cdot (Z - Z_{geo}) \cdot h_{bbox} = \frac{Z_{err} \cdot h_{bbox}}{f} \quad (7)$$

As illustrated in Fig. 4(b), when the object rotates around the center point, Z_{err} will fluctuate in tandem with h_{bbox} , leading to an amplification effect on the distribution of H_{err} . Similar to the squaring operation in the chi-square distribution, the multiplication in Eq. (7) introduces nonlinear transformation, resulting in a skewed data distribution.

(2) Bounding box height error h_{err} : Compared with other geometry errors, h_{err} is located in the denominator of the modified Eq. (6). Its gradient calculation formula can be expressed as:

$$\frac{\partial L_{depth}}{\partial h_{err}} = \frac{\partial L_{depth}}{\partial Z} \cdot \frac{f \cdot H}{(h_{bbox} - h_{err})^2} \quad (8)$$

During the backpropagation process, the gradient calculations on h_{err} are non-linear and unstable, thus increasing the difficulty of model training and convergence.

In summary, we obtain Z_{geo} using h_{bbox} instead of h_c and select Z_{err} to compensate the projection formula. These measures can greatly optimize data distribution and reduce the model’s learning costs. The difficulty of predicting depth-related attributes is ranked as follows:

$$Z > h_{err} > H_{err} > Z_{err} \approx H \gg h_{bbox} \quad (9)$$

Methods	Extra data	Reference	Test, $AP_{BEV R40}$			Test, $AP_{3D R40}$			Val, $AP_{BEV R40}$			Val, $AP_{3D R40}$		
			Easy	Mod.	Hard	Easy	Mod.	Hard	Easy	Mod.	Hard	Easy	Mod.	Hard
CaDDN [43]	LiDAR	CVPR 2021	27.94	18.91	17.19	19.17	13.41	11.46	-	-	-	23.57	16.31	13.84
MonoDTR [17]		CVPR 2022	28.59	20.38	17.14	21.99	15.39	12.73	33.33	25.35	21.68	24.52	18.57	15.51
DID-M3D [38]		ECCV 2022	32.95	22.76	19.83	24.40	16.29	13.75	31.10	22.76	19.50	22.98	16.12	14.03
OccupancyM3D [39]		CVPR 2024	35.38	24.18	21.37	<u>25.55</u>	17.02	14.79	35.72	26.60	23.68	26.87	19.96	<u>17.15</u>
MonoPGC [57]	Depth	ICRA 2023	32.50	23.14	20.30	24.68	<u>17.17</u>	14.14	34.06	24.26	20.78	25.67	18.63	15.65
OPA-3D [51]		RAL 2023	33.54	22.53	19.22	24.60	17.05	14.25	33.80	25.51	22.13	24.97	19.40	16.59
GUPNet [33]	None	ICCV 2021	-	-	-	20.11	14.20	11.77	31.07	22.94	19.75	22.76	16.46	13.72
MonoCon [30]		AAAI 2022	31.12	22.10	19.00	22.50	16.46	13.95	-	-	-	26.33	19.01	15.98
DEVIANT [21]		ECCV 2022	29.65	20.44	17.43	21.88	14.46	11.89	32.60	23.04	19.99	24.63	16.54	14.52
MonoDDE [26]		CVPR 2022	33.58	23.46	20.37	24.93	17.14	<u>15.10</u>	35.51	26.48	23.07	26.66	19.75	16.72
MonoUNI [18]		NeurIPS 2023	-	-	-	24.75	16.73	13.49	-	-	-	24.51	17.18	14.01
MonoDETR [62]		ICCV 2023	33.60	22.11	18.60	25.00	16.47	13.58	37.86	<u>26.95</u>	22.80	28.84	<u>20.61</u>	16.38
MonoCD [60]		CVPR 2024	33.41	22.81	19.57	25.53	16.59	14.53	34.60	24.96	21.51	26.45	19.37	16.38
FD3D [58]		AAAI 2024	34.20	23.72	20.76	25.38	17.12	14.50	36.98	26.77	23.16	28.22	20.23	17.04
Ours		None	-	<u>35.24</u>	25.23	22.02	26.35	18.72	15.97	39.40	28.20	24.42	30.76	22.34
Improvement	-	-	-0.14	+1.05	+0.65	+0.80	+1.55	+0.87	+1.54	+1.25	+1.33	+1.92	+1.73	+1.87

Table 1. Comparisons with state-of-the-art monocular methods on the KITTI test and val sets for the car category. We **bold** the best results and underline the second-best results. The **blue** refers to the gain and the **red** is the decrease of our method.

3.6. Loss Function

The training loss consists of four distinct components: region loss L_{region} , depth map loss L_{dmap} , 2D loss L_{2D} , and 3D loss L_{3D} . Specifically, L_{2D} contains the losses of object category, bounding box, GIoU, and projected center point, while L_{3D} includes the losses of 3D size, orientation, and central depth. We denote the weights of 2D and 3D losses from λ_1 to λ_7 . The overall loss is formulated as:

$$L_{overall} = L_{2D} + L_{3D} + \lambda_8 L_{dmap} + \lambda_9 \sum_{i=0}^4 L_{region}^i \quad (10)$$

4. Experiments

4.1. Settings

Dataset. We select the widely used KITTI benchmark [14] to evaluate our proposed model. This 3D object detection benchmark consists of 7481 training images and 7518 testing images. It has three difficulty levels (Easy, Moderate, and Hard) and three classes (Car, Pedestrian, and Cyclist). According to the prior work [10], we divide the 7481 training images into a training set with 3712 images and a validation set with 3769 images for ablation study.

Evaluation Metrics. We present the detection outcomes categorized by three difficulty levels: easy, moderate, and hard. Consistent with prior works, our evaluation relies on average precision (AP) metrics for both 3D bounding boxes and bird’s-eye view, referred to as AP_{3D} and AP_{BEV} , which are calculated at 40 recall positions following the established protocol [50]. The benchmark ranks all methods based on the moderate AP_{3D} metrics of “Car” category.

Implementation Details. We take ResNet50 [15] as our backbone. In regard to Transformer, we adopt 8 heads in each attention module and set the number of queries 50 with 4 sampling points in the multi-scale deformable attention.

Methods	Val, Mod. AP_{3D}	Params (M)↓	FLOPs (G)↓	Runtime (ms)↓
Baseline	20.22	35.93	59.72	35
MonoDGP (Ours)	22.34	38.90	68.99	42
w/o Decoupled Query	21.48	37.54	65.75	39
w/o RSH	21.93	36.23	62.25	37

Table 2. Ablation study of computational cost. We test the Runtime (ms) on a single RTX 3090 GPU with a batch size of 1.

The weights of losses are set as $\{2, 5, 2, 10, 1, 1, 1, 1, 1\}$ for λ_1 to λ_9 . On a single RTX 3090 GPU, using Mixup3D [27], we train MonoDGP for 250 epochs with a batch size of 8 and a learning rate of $2e-4$. We utilize AdamW [32] optimizer with weight decay and decrease learning rate by a factor of 0.5 at epochs 85, 125, 165, and 225. To accelerate the model’s convergence, we adopt group-wise one-to-many assignment [9] with 11 groups. During inference, we filter out queries with category confidence lower than 0.2.

4.2. Main Results

To present the performance of our proposed method, we provide quantitative results on the KITTI test and val splits.

As shown in Tab. 1, we have compared advanced monocular 3D detectors in recent years. Without additional data, MonoDGP comprehensively surpasses the baseline model MonoDETR [62] and achieves competitive results across most metrics. In particular, our method improves moderate AP_{3D} by up to 1.55% on the test set and 1.73% on the validation set, respectively. Except that easy AP_{BEV} on test set achieves the second-best lower than OccupancyM3D [39], which introduces extra data during the training phase, other metrics all reach the state-of-the-art performance.

It should be noted that we employ early stopping to select the best validation checkpoint, while we directly select the last few checkpoints for test submission. To mitigate the

Segment Embeddings Threshold	Val, $AP_{3D R40}$		
	Easy	Mod.	Hard
0.3	29.77	21.51	18.35
0.5	30.57	21.64	18.74
0.7	30.35	21.54	18.55
w/o	29.63	21.43	18.21

Table 3. The design of region segmentation head. “w/o” denotes enhancing visual and depth features without segment embeddings.

Depth Prediction Mode	Val, $AP_{3D R40}$		
	Easy	Mod.	Hard
Depth Map	24.33	18.87	15.31
Direct Depth	26.60	19.23	16.47
Geometric Depth (h_{bbox})	9.15	7.99	5.52
Geometric Depth (h_c)	27.63	20.73	18.04
Weighted Fusion	30.57	21.64	18.74
GD + Bbox Height Error	28.45	21.18	17.91
GD + Dim Height Error	30.46	22.09	18.85
GD + Depth Error	30.76	22.34	19.01

Table 4. Ablation study of different depth prediction modes on KITTI val set. The weighted fusion mode integrates the results from the depth map, direct depth, and geometric depth (h_{bbox}). “GD” denotes the geometric depth calculated by the formula $Z_{geo} = f \times H_{3D}/h_{bbox}$.

instability of the DETR-based method, all ablation studies follow the same protocol where models are trained 5 times on val set with median moderate AP_{3D} reported.

4.3. Ablation Study

Computational cost. We analyze the computational costs of the main modules in Tab. 2 (Depth Error does not incur additional computation). Although the decoupled query and RSH modules introduce a slight increase in computational overhead, they greatly improve the performance. Our complete network achieves a runtime of 42 ms, which is comparable to recent state-of-the-art methods such as MonoCD [60] (36 ms) and OccupancyM3D [39] (112 ms).

Region segmentation head. For the multi-scale target region probabilities predicted by RSH, we set distinct thresholds to produce segment embeddings, which serve as input tokens for the depth encoder. The results are presented in Tab. 3. The segment embeddings strength encoders’ ability to comprehend the contextual relationships among image pixels. Experiments further highlight the critical role of segment embeddings. Moreover, the threshold settings also influence 3D evaluation metrics. A threshold of 0.5 achieves superior results compared to other thresholds.

Depth prediction mode. Based on the same network, we compare different depth prediction modes in Tab. 4. The experiment indicates that single depth predictions, whether using direct depth, depth map, or geometric depth (h_{bbox} or h_c), generally perform poorly, especially for geometric depth (h_{bbox}). Considering only perspective transformation

Mixup3D	Decoupled Query	Region Segment	Geometric Depth Error	Val, $AP_{3D R40}$		
				Easy	Mod.	Hard
✗	✗	✗	✗	26.56	20.22	17.21
✓	✗	✗	✗	28.17	20.79	17.52
✓	✓	✗	✗	29.82	21.38	18.04
✓	✓	✓	✗	30.57	21.64	18.74
✓	✓	✗	✓	30.08	21.93	18.87
✓	✗	✓	✓	28.91	21.48	18.43
✓	✓	✓	✓	30.76	22.34	19.01
Improvement				+ 4.20	+2.12	+1.80

Table 5. The main ablation study.

on the visual surface, the moderate AP_{3D} for geometric depth (h_{bbox}) is just 7.99% (all AP_{3D} mentioned below default to the moderate level), significantly lower than other prediction modes. By fusing direct depth, depth map and geometric depth, the AP_{3D} improves to 21.64%. When geometry errors are added to compensate for the projection formula, it can be observed that the performance achieves a substantial increase. The depth error wins the best performance with an AP_{3D} of 22.34%. The dimension height error comes second at 22.09% due to its skewed distribution. The bounding box height error only acquires 21.18% in AP_{3D} , obviously inferior to other geometry errors. This discrepancy can be attributed to the non-linearity of the gradient backpropagation calculation.

Overall performance. We explore the impact of each improvement technique on the baseline. The main ablation study is shown in Tab. 5. The MonoDGP employs four key techniques: mixup3D augmentation, decoupling and initialization of 2D object queries, region enhancement with segment embeddings, and depth error prediction based on geometric depth. Compared to the baseline, the AP_{3D} under three-level difficulties gain an increase by +4.20%, +2.12% and +1.80%, respectively. These experiments validate the effectiveness of each technique utilized in MonoDGP.

5. Conclusion

In this paper, we propose a novel transformer-based monocular method called MonoDGP, which adopts geometry errors to correct the projection formula. We also comprehensively analyze the properties and effectiveness of geometry errors, from the perspectives of marginal feature extraction, data distribution, and gradient propagation. Error prediction is expected to become a better alternative to multi-depth prediction, without complex multi-branch implementations. Furthermore, MonoDGP introduces a 2D visual decoder for query initialization and a region segmentation head for feature enhancement. These improvements have achieved superior performance on the KITTI benchmark. We can also extend our approach to dense depth map prediction for the target region, by only considering errors between geometric depth and surface points of the objects.

References

- [1] Wentao Bao, Qi Yu, and Yu Kong. Object-aware centroid voting for monocular 3d object detection. In *2020 IEEE/RSJ international conference on intelligent robots and systems (IROS)*, pages 2197–2204. IEEE, 2020. 2
- [2] Ivan Barabanau, Alexey Artemov, Evgeny Burnaev, and Vyacheslav Murashkin. Monocular 3d object detection via geometric reasoning on keypoints. *arXiv preprint arXiv:1905.05618*, 2019. 2
- [3] Ivan Barabanau, Alexey Artemov, Evgeny Burnaev, and Vyacheslav Murashkin. Monocular 3d object detection via geometric reasoning on keypoints. *arXiv preprint arXiv:1905.05618*, 2019. 13
- [4] Garrick Brazil and Xiaoming Liu. M3d-rpn: Monocular 3d region proposal network for object detection. In *ICCV*, pages 9287–9296, 2019. 15
- [5] Garrick Brazil, Gerard Pons-Moll, Xiaoming Liu, and Bernt Schiele. Kinematic 3d object detection in monocular video. In *ECCV*, pages 135–152. Springer, 2020. 2
- [6] Yohann Cabon, Naila Murray, and Martin Humenberger. Virtual kitti 2. *arXiv preprint arXiv:2001.10773*, 2020. 14
- [7] Yingjie Cai, Buyu Li, Zeyu Jiao, Hongsheng Li, Xingyu Zeng, and Xiaogang Wang. Monocular 3d object detection with decoupled structured polygon estimation and height-guided depth estimation. In *AAAI*, pages 10478–10485, 2020. 2
- [8] Nicolas Carion, Francisco Massa, Gabriel Synnaeve, Nicolas Usunier, Alexander Kirillov, and Sergey Zagoruyko. End-to-end object detection with transformers. In *European conference on computer vision*, pages 213–229. Springer, 2020. 2
- [9] Qiang Chen, Xiaokang Chen, Jian Wang, Shan Zhang, Kun Yao, Haocheng Feng, Junyu Han, Errui Ding, Gang Zeng, and Jingdong Wang. Group detr: Fast detr training with group-wise one-to-many assignment. In *Proceedings of the IEEE/CVF International Conference on Computer Vision*, pages 6633–6642, 2023. 7
- [10] Xiaozhi Chen, Kaustav Kundu, Yukun Zhu, Andrew G Berneshawi, Huimin Ma, Sanja Fidler, and Raquel Urtasun. 3d object proposals for accurate object class detection. *NeurIPS*, 28, 2015. 7
- [11] Xiaozhi Chen, Kaustav Kundu, Ziyu Zhang, Huimin Ma, Sanja Fidler, and Raquel Urtasun. Monocular 3d object detection for autonomous driving. In *CVPR*, pages 2147–2156, 2016. 2
- [12] Yilun Chen, Shijia Huang, Shu Liu, Bei Yu, and Jiaya Jia. Dsgn++: Exploiting visual-spatial relation for stereo-based 3d detectors. *IEEE Transactions on Pattern Analysis and Machine Intelligence*, 45(4):4416–4429, 2022. 1
- [13] Tom van Dijk and Guido de Croon. How do neural networks see depth in single images? In *Proceedings of the IEEE/CVF International Conference on Computer Vision*, pages 2183–2191, 2019. 2
- [14] Andreas Geiger, Philip Lenz, and Raquel Urtasun. Are we ready for autonomous driving? the kitti vision benchmark suite. In *CVPR*, pages 3354–3361. IEEE, 2012. 7
- [15] Kaiming He, Xiangyu Zhang, Shaoqing Ren, and Jian Sun. Deep residual learning for image recognition. In *Proceedings of the IEEE conference on computer vision and pattern recognition*, pages 770–778, 2016. 7
- [16] Jie Hu, Li Shen, and Gang Sun. Squeeze-and-excitation networks. In *Proceedings of the IEEE conference on computer vision and pattern recognition*, pages 7132–7141, 2018. 4
- [17] Kuan-Chih Huang, Tsung-Han Wu, Hung-Ting Su, and Winston H Hsu. Monodr: Monocular 3d object detection with depth-aware transformer. In *CVPR*, pages 4012–4021, 2022. 2, 7
- [18] Jia Jinrang, Zhenjia Li, and Yifeng Shi. Monouni: A unified vehicle and infrastructure-side monocular 3d object detection network with sufficient depth clues. *Advances in Neural Information Processing Systems*, 36:11703–11715, 2023. 7, 15
- [19] Jacob Devlin Ming-Wei Chang Kenton and Lee Kristina Toutanova. Bert: Pre-training of deep bidirectional transformers for language understanding. In *Proceedings of naacL-HLT*, page 2. Minneapolis, Minnesota, 2019. 2, 4
- [20] Jason Ku, Alex D Pon, and Steven L Waslander. Monocular 3d object detection leveraging accurate proposals and shape reconstruction. In *CVPR*, pages 11867–11876, 2019. 2
- [21] Abhinav Kumar, Garrick Brazil, Enrique Corona, Armin Parchami, and Xiaoming Liu. Deviant: Depth equivariant network for monocular 3d object detection. In *ECCV*, pages 664–683. Springer, 2022. 7, 14, 15
- [22] Alex H Lang, Sourabh Vora, Holger Caesar, Lubing Zhou, Jiong Yang, and Oscar Beijbom. Pointpillars: Fast encoders for object detection from point clouds. In *CVPR*, pages 12697–12705, 2019. 1
- [23] Peiliang Li, Xiaozhi Chen, and Shaojie Shen. Stereo r-cnn based 3d object detection for autonomous driving. In *CVPR*, pages 7644–7652, 2019. 1
- [24] Peixuan Li, Shun Su, and Huaici Zhao. Rts3d: Real-time stereo 3d detection from 4d feature-consistency embedding space for autonomous driving. In *AAAI*, pages 1930–1939, 2021. 1
- [25] Yingyan Li, Yuntao Chen, Jiawei He, and Zhaoxiang Zhang. Densely constrained depth estimator for monocular 3d object detection. In *ECCV*, pages 718–734. Springer, 2022. 2
- [26] Zhuoling Li, Zhan Qu, Yang Zhou, Jianzhuang Liu, Haoqian Wang, and Lihui Jiang. Diversity matters: Fully exploiting depth clues for reliable monocular 3d object detection. In *CVPR*, pages 2791–2800, 2022. 1, 2, 3, 7, 14
- [27] Zhenjia Li, Jinrang Jia, and Yifeng Shi. Monolss: Learnable sample selection for monocular 3d detection. In *2024 International Conference on 3D Vision (3DV)*, pages 1125–1135. IEEE, 2024. 7
- [28] Tsung-Yi Lin, Priya Goyal, Ross Girshick, Kaiming He, and Piotr Dollár. Focal loss for dense object detection. In *2017 IEEE International Conference on Computer Vision (ICCV)*, pages 2999–3007, 2017. 13
- [29] Lijie Liu, Chufan Wu, Jiwen Lu, Lingxi Xie, Jie Zhou, and Qi Tian. Reinforced axial refinement network for monocular 3d object detection. In *Computer Vision—ECCV 2020: 16th European Conference, Glasgow, UK, August 23–28, 2020, Proceedings, Part XVII 16*, pages 540–556. Springer, 2020. 2

- [30] Xianpeng Liu, Nan Xue, and Tianfu Wu. Learning auxiliary monocular contexts helps monocular 3d object detection. In *AAAI*, pages 1810–1818, 2022. [2](#), [7](#), [14](#)
- [31] Zechen Liu, Zizhang Wu, and Roland Tóth. Smoke: Single-stage monocular 3d object detection via keypoint estimation. In *CVPRW*, pages 996–997, 2020. [2](#)
- [32] Ilya Loshchilov and Frank Hutter. Decoupled weight decay regularization. In *International Conference on Learning Representations*, 2018. [7](#)
- [33] Yan Lu, Xinzhu Ma, Lei Yang, Tianzhu Zhang, Yating Liu, Qi Chu, Junjie Yan, and Wanli Ouyang. Geometry uncertainty projection network for monocular 3d object detection. In *ICCV*, pages 3111–3121, 2021. [2](#), [3](#), [7](#), [13](#), [14](#), [15](#)
- [34] Xinzhu Ma, Shinan Liu, Zhiyi Xia, Hongwen Zhang, Xingyu Zeng, and Wanli Ouyang. Rethinking pseudo-lidar representation. In *Proceedings of the European Conference on Computer Vision (ECCV)*, 2020. [15](#)
- [35] Xinzhu Ma, Yinmin Zhang, Dan Xu, Dongzhan Zhou, Shuai Yi, Haojie Li, and Wanli Ouyang. Delving into localization errors for monocular 3d object detection. In *CVPR*, pages 4721–4730, 2021. [13](#)
- [36] Arsalan Mousavian, Dragomir Anguelov, John Flynn, and Jana Kosecka. 3d bounding box estimation using deep learning and geometry. In *Proceedings of the IEEE conference on Computer Vision and Pattern Recognition*, pages 7074–7082, 2017. [1](#), [13](#)
- [37] Andretti Naiden, Vlad Paunescu, Gyeongmo Kim, Byeong-Moon Jeon, and Marius Leordeanu. Shift r-cnn: Deep monocular 3d object detection with closed-form geometric constraints. In *2019 IEEE international conference on image processing (ICIP)*, pages 61–65. IEEE, 2019. [2](#), [13](#)
- [38] Liang Peng, Xiaopei Wu, Zheng Yang, Haifeng Liu, and Deng Cai. Did-m3d: Decoupling instance depth for monocular 3d object detection. In *ECCV*, pages 71–88. Springer, 2022. [1](#), [2](#), [7](#)
- [39] Liang Peng, Junkai Xu, Haoran Cheng, Zheng Yang, Xiaopei Wu, Wei Qian, Wenxiao Wang, Boxi Wu, and Deng Cai. Learning occupancy for monocular 3d object detection. In *Proceedings of the IEEE/CVF Conference on Computer Vision and Pattern Recognition*, pages 10281–10292, 2024. [2](#), [7](#), [8](#), [14](#)
- [40] Xidong Peng, Xinge Zhu, Tai Wang, and Yuexin Ma. Side-center-based stereo 3d detector with structure-aware instance depth estimation. In *Proceedings of the IEEE/CVF Winter Conference on Applications of Computer Vision*, pages 119–128, 2022. [1](#)
- [41] Rui Qian, Xin Lai, and Xirong Li. 3d object detection for autonomous driving: A survey. *Pattern Recognition*, 130: 108796, 2022. [1](#)
- [42] Zequn Qin and Xi Li. Monoground: Detecting monocular 3d objects from the ground. In *CVPR*, pages 3793–3802, 2022. [1](#)
- [43] Cody Reading, Ali Harakeh, Julia Chae, and Steven L Waslander. Categorical depth distribution network for monocular 3d object detection. In *CVPR*, pages 8555–8564, 2021. [2](#), [7](#), [14](#), [15](#)
- [44] Mike Roberts, Jason Ramapuram, Anurag Ranjan, Atulit Kumar, Miguel Angel Bautista, Nathan Paczan, Russ Webb, and Joshua M Susskind. Hypersim: A photorealistic synthetic dataset for holistic indoor scene understanding. In *Proceedings of the IEEE/CVF international conference on computer vision*, pages 10912–10922, 2021. [14](#)
- [45] Olaf Ronneberger, Philipp Fischer, and Thomas Brox. U-net: Convolutional networks for biomedical image segmentation. In *Medical image computing and computer-assisted intervention—MICCAI 2015: 18th international conference, Munich, Germany, October 5–9, 2015, proceedings, part III 18*, pages 234–241. Springer, 2015. [3](#)
- [46] Shaoshuai Shi, Chaoxu Guo, Li Jiang, Zhe Wang, Jianping Shi, Xiaogang Wang, and Hongsheng Li. Pv-rcnn: Point-voxel feature set abstraction for 3d object detection. In *CVPR*, pages 10529–10538, 2020. [1](#)
- [47] Shaoshuai Shi, Li Jiang, Jiajun Deng, Zhe Wang, Chaoxu Guo, Jianping Shi, Xiaogang Wang, and Hongsheng Li. Pv-rcnn++: Point-voxel feature set abstraction with local vector representation for 3d object detection. *International Journal of Computer Vision*, 131(2):531–551, 2023. [1](#)
- [48] Xuepeng Shi, Qi Ye, Xiaozhi Chen, Chuangrong Chen, Zhixiang Chen, and Tae-Kyun Kim. Geometry-based distance decomposition for monocular 3d object detection. In *ICCV*, pages 15172–15181, 2021. [2](#)
- [49] Yuguang Shi, Yu Guo, Zhenqiang Mi, and Xinjie Li. Stereo centernet-based 3d object detection for autonomous driving. *Neurocomputing*, 471:219–229, 2022. [1](#)
- [50] Andrea Simonelli, Samuel Rota Buló, Lorenzo Porzi, Manuel López-Antequera, and Peter Kontschieder. Disentangling monocular 3d object detection. In *ICCV*, pages 1991–1999, 2019. [2](#), [7](#)
- [51] Yongzhi Su, Yan Di, Guangyao Zhai, Fabian Manhardt, Jason Rambach, Benjamin Busam, Didier Stricker, and Federico Tombari. Opa-3d: Occlusion-aware pixel-wise aggregation for monocular 3d object detection. *IEEE Robotics and Automation Letters*, 8(3):1327–1334, 2023. [7](#)
- [52] Pei Sun, Henrik Kretzschmar, Xerxes Dotiwalla, Aurelien Chouard, Vijaysai Patnaik, Paul Tsui, James Guo, Yin Zhou, Yuning Chai, Benjamin Caine, et al. Scalability in perception for autonomous driving: Waymo open dataset. In *Proceedings of the IEEE/CVF conference on computer vision and pattern recognition*, pages 2446–2454, 2020. [14](#)
- [53] Ashish Vaswani, Noam Shazeer, Niki Parmar, Jakob Uszkoreit, Llion Jones, Aidan N Gomez, Łukasz Kaiser, and Illia Polosukhin. Attention is all you need. *NeurIPS*, 30, 2017. [2](#)
- [54] Li Wang, Liang Du, Xiaoqing Ye, Yanwei Fu, Guodong Guo, Xiangyang Xue, Jianfeng Feng, and Li Zhang. Depth-conditioned dynamic message propagation for monocular 3d object detection. In *CVPR*, pages 454–463, 2021. [2](#)
- [55] Li Wang, Li Zhang, Yi Zhu, Zhi Zhang, Tong He, Mu Li, and Xiangyang Xue. Progressive coordinate transforms for monocular 3d object detection. *Advances in Neural Information Processing Systems*, 34:13364–13377, 2021. [15](#)
- [56] Tai Wang, ZHU Xinge, Jiangmiao Pang, and Dahua Lin. Probabilistic and geometric depth: Detecting objects in perspective. In *Conference on Robot Learning*, pages 1475–1485. PMLR, 2022. [2](#)
- [57] Zizhang Wu, Yuanzhu Gan, Lei Wang, Guilian Chen, and Jian Pu. Monopgc: Monocular 3d object detection with

- pixel geometry contexts. In *2023 IEEE International Conference on Robotics and Automation (ICRA)*, pages 4842–4849. IEEE, 2023. [2](#), [7](#), [14](#)
- [58] Zizhang Wu, Yuanzhu Gan, Yunzhe Wu, Ruihao Wang, Xiaoguan Wang, and Jian Pu. Fd3d: Exploiting foreground depth map for feature-supervised monocular 3d object detection. In *Proceedings of the AAAI Conference on Artificial Intelligence*, pages 6189–6197, 2024. [7](#)
- [59] Qiangeng Xu, Yiqi Zhong, and Ulrich Neumann. Behind the curtain: Learning occluded shapes for 3d object detection. In *AAAI*, pages 2893–2901, 2022. [1](#)
- [60] Longfei Yan, Pei Yan, Shengzhou Xiong, Xuanyu Xiang, and Yihua Tan. Monocd: Monocular 3d object detection with complementary depths. In *Proceedings of the IEEE/CVF Conference on Computer Vision and Pattern Recognition*, pages 10248–10257, 2024. [2](#), [3](#), [7](#), [8](#)
- [61] Lihe Yang, Bingyi Kang, Zilong Huang, Zhen Zhao, Xiaogang Xu, Jiashi Feng, and Hengshuang Zhao. Depth anything v2. *Advances in Neural Information Processing Systems*, 37:21875–21911, 2025. [14](#)
- [62] Renrui Zhang, Han Qiu, Tai Wang, Ziyu Guo, Ziteng Cui, Yu Qiao, Hongsheng Li, and Peng Gao. Monodetr: Depth-guided transformer for monocular 3d object detection. In *ICCV*, pages 9155–9166, 2023. [2](#), [3](#), [7](#), [13](#), [14](#)
- [63] Yunpeng Zhang, Jiwen Lu, and Jie Zhou. Objects are different: Flexible monocular 3d object detection. In *CVPR*, pages 3289–3298, 2021. [1](#), [2](#)
- [64] Yunsong Zhou, Yuan He, Hongzi Zhu, Cheng Wang, Hongyang Li, and Qinrong Jiang. Monocular 3d object detection: An extrinsic parameter free approach. In *Proceedings of the IEEE/CVF Conference on Computer Vision and Pattern Recognition*, pages 7556–7566, 2021. [2](#)
- [65] Yunsong Zhou, Hongzi Zhu, Quan Liu, Shan Chang, and Minyi Guo. Monoatt: Online monocular 3d object detection with adaptive token transformer. In *CVPR*, pages 17493–17503, 2023. [2](#)
- [66] Minghan Zhu, Lingting Ge, Panqu Wang, and Huei Peng. Monoedge: Monocular 3d object detection using local perspectives. In *Proceedings of the IEEE/CVF Winter Conference on Applications of Computer Vision*, pages 643–652, 2023. [1](#)
- [67] Xizhou Zhu, Weijie Su, Lewei Lu, Bin Li, Xiaogang Wang, and Jifeng Dai. Deformable detr: Deformable transformers for end-to-end object detection. *arXiv preprint arXiv:2010.04159*, 2020. [4](#)

MonoDGP: Monocular 3D Object Detection with Decoupled-Query and Geometry-Error Priors

Supplementary Material

A. Detailed Discussion on Depth Error

In our method, we regard the distance between the camera plane and the car's closest wheel point as the geometric depth. However, this assumption is appropriate when the camera has the same height of the object. The height inconsistency will lead to the bias l_{bias} between the actual geometric depth Z_{geo} and the wheel depth Z_w . We set the height ratio γ of the camera height H_{cam} to the object height H as follows:

$$\gamma = \frac{H_{cam}}{H} \quad (11)$$

We will discuss how the height ratio affects the distribution of the depth error Z_{err} .

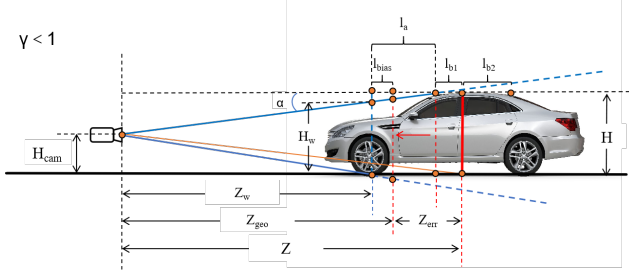


Figure 7. The perspective transformation when the camera height is lower than the object height.

The vehicle is treated as a trapezoid. The closest wheel locates in the lowest position of the 2D bounding box, while the highest position in the object surface will change with the height ratio. As shown in Fig. 7, when $\gamma < 1$, the wheel depth is shorter than the geometric depth, which can be expressed as:

$$Z_{geo} = Z_w + l_{bias} \quad (12)$$

To calculate the wheel bias, we first represent the height at the wheel point based on the similar triangle theory:

$$\tan\alpha = \frac{H - H_{cam}}{Z_w + l_a} = \frac{H - H_w}{l_a} \quad (13)$$

$$H_w = H - \frac{(H - H_{cam}) \cdot l_a}{Z_w + l_a} \quad (14)$$

And then we utilize H_w to compute l_{bias} :

$$\frac{H}{Z_{geo}} = \frac{H_w}{Z_w} \quad (15)$$

$$l_{bias} = \frac{(H - H_{cam}) \cdot Z_w \cdot l_a}{H \cdot Z_w + H_{cam} \cdot l_a} = \frac{(1 - \gamma) \cdot Z_w \cdot l_a}{Z_w + \gamma \cdot l_a} \quad (16)$$

We can express depth error as follows:

$$Z_{err} = l_{b1} + l_a - l_{bias} = l_{b1} + \sigma_1 \cdot l_a \quad (17)$$

$$\sigma_1 = \frac{\gamma}{1 - \frac{(1-\gamma) \cdot l_a}{Z_w + l_a}} \quad (18)$$

where $\gamma < \sigma_1 < 1$, $l_{bias} < (1 - \gamma) \cdot l_a$. The original depth error, which should be perspective-invariant, is calculated by the formula $Z_{err} = l_{b1} + l_a$. Except for the vehicle's own attributes, γ and Z_w also affect the depth error. The closer σ_1 is to 1, the less effect it has. According to the Eq. (18), σ_1 reduces as Z_w increases and γ decreases.

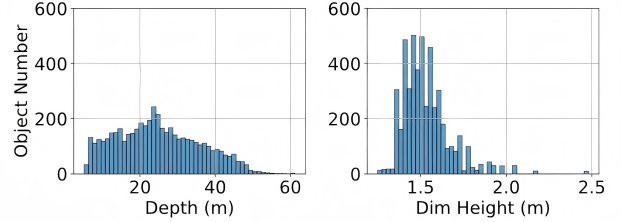


Figure 8. The data distribution of the object's central depth and dimension height on the KITTI training set.

To present the greatest impact of the height ratio, we take an extreme example based on the Fig. 8, and make σ_1 as smaller as possible. Specifically, we set $H_{cam} = 1.5m$, $H = 1.8m$, $\gamma = \frac{5}{6}$, $l_a = 1m$, $Z_w = 50m$. From the Eq. (16) and Eq. (18), we obtain $\sigma_1 \approx 0.84$ and $l_{bias} \approx 0.16m$. This extreme bias value is significantly lower than the whole depth value.

As shown in Fig. 9, when $\gamma > 1$, the wheel depth is larger than the geometric depth, which can be expressed as:

$$Z_{geo} = Z_w - l_{bias} \quad (19)$$

We can achieve the wheel bias similar to the previous proof process:

$$\tan\beta = \frac{H_{cam} - H}{Z_w + l_a + l_{b1} + l_{b2}} = \frac{H_w - H}{l_a + l_{b1} + l_{b2}} \quad (20)$$

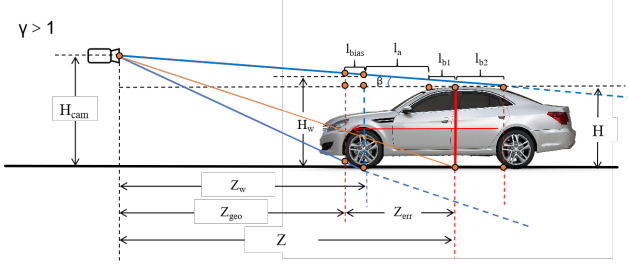


Figure 9. The perspective transformation when the camera height is higher than the object height.

$$H_w = \frac{H \cdot Z_w + H_{cam} \cdot (l_a + l_{b1} + l_{b2})}{Z_w + l_a + l_{b1} + l_{b2}} \quad (21)$$

$$l_{bias} = \frac{(\gamma - 1) \cdot Z_w \cdot (l_a + l_{b1} + l_{b2})}{Z_w + \gamma \cdot (l_a + l_{b1} + l_{b2})} \quad (22)$$

Homogeneously, we can express depth error as follows:

$$Z_{err} = l_{b1} + l_a + \sigma_2 \cdot (l_a + l_{b1} + l_{b2}) \quad (23)$$

$$\sigma_2 = \frac{(\gamma - 1)}{1 + \frac{\gamma \cdot (l_a + l_{b1} + l_{b2})}{Z_w}} \quad (24)$$

where $0 < \sigma_2 < \gamma - 1$, $l_{bias} < (\gamma - 1) \cdot (l_a + l_{b1} + l_{b2})$. The closer σ_2 is to 0, the less effect it has. According to the Eq. (24), σ_2 increases as Z_w and γ increase.

To show the height ratio's maximum impact, we also suppose an extreme case and make σ_2 as larger as possible. To be more specific, we set $H_{cam} = 1.5m$, $H = 1.25m$, $\gamma = \frac{6}{5}$, $l_a + l_{b1} + l_{b2} = 2m$, $Z_w = 50m$. Based on the Eq. (22) and Eq. (24), we achieve $\sigma_2 \approx 0.19$ and $l_{bias} \approx 0.38m$. This bias value is higher than the value calculated when $\gamma < 1$, but has a slight effect on the whole depth.

In most instances, the camera height is close to the vehicle height, which means $\gamma \approx 1$ and the depth error is roughly perspective-invariant for the car category. Even if the object height is obviously different from the camera height, the network can directly learn and predict this tiny bias compared with the whole depth. The error prediction is still a simple and effective method to replace the multi-depth prediction.

B. Discussion on Geometric Constraints

Previous works like Deep3DBox [36] and Shift R-CNN [37] enforce strict geometric constraints by tightly fitting projections of the 3D bounding box into the 2D box. While recent methods such as MonoGR2 [3] and GUP-Net [33] formulate constraints based on geometric similarity, where under vehicle-mounted camera perspectives and

fixed focal length, the object's center depth can be uniquely determined through the proportional relationship between its 3D height and 2D projected height.

Projection-alignment constraints exhibit quadratic errors from 2D boundary localization inaccuracies, while height-ratio constraints demonstrate linear errors confined to height predictions. The former fails with truncated objects requiring full 2D contours, whereas the latter maintains functionality under partial occlusions through visible height segments. Height-ratio constraints surpass projection-alignment methods in stability (linear vs. quadratic errors), efficiency (closed-form vs. iterative), and robustness (partial vs. full contours), establishing them as core geometric priors for monocular 3D detection. Future frameworks could incorporate projection-alignment constraints as auxiliary regularizers within joint optimization.

C. Detailed Loss Function

The 2D loss L_{2D} adopts focal loss [28] to estimate the object categories, L1 loss to estimate the projected center (x_{3d}, y_{3d}) and 2D sizes (l, r, t, b) , and GIoU loss for the bounding box. We can formulate the 2D object loss as:

$$L_{2D} = \lambda_1 L_{cls} + \lambda_2 L_{2dsize} + \lambda_3 L_{xy} + \lambda_4 L_{giou} \quad (25)$$

The 3D loss follows MonoDLE [35] to predict 3D sizes (h_{3d}, w_{3d}, l_{3d}) and orientation angle α . As for the depth prediction, an uncertainty regression loss based on the Laplacian distribution is defined as:

$$L_{depth} = \frac{\sqrt{2}}{\sigma_d} \left\| \frac{f \cdot H}{h_{bbox}} + Z_{err} - Z_{gt} \right\|_1 + \log(\sigma_d) \quad (26)$$

where σ_d is the standard deviation of the distribution.

We can formulate 3D object loss as:

$$L_{3D} = \lambda_5 L_{3dsize} + \lambda_6 L_{angle} + \lambda_7 L_{depth} \quad (27)$$

The depth map loss L_{dmap} utilizes focal loss to predict categorical foreground depth map. More detailed information about L_{dmap} can be found in MonoDETR [62].

D. Experiments on Other Categories

Since segment embeddings are mainly trained to distinguish between background and target, they can easily handle multiple classes without modification. Ablation studies of other categories are shown in Tab. 6. In particular, error prediction significantly improves 3D pedestrian prediction compared to cars and cyclists. This can be explained that pedestrians have consistent depth errors across orientations, whereas cyclists have irregular shapes and greater geometric uncertainty. These spatial uncertainties may degrade the effectiveness of the projection transformation.

Methods	Val, IoU=0.5, $AP_{3D R40}$					
	Pedestrian			Cyclist		
	Easy	Mod.	Hard	Easy	Mod.	Hard
MonoDGP (Ours)	13.77	10.06	7.96	12.21	6.61	5.95
w/o Segment Embeddings	13.02	9.67	7.66	10.56	5.22	4.68
w/o RSH	12.50	9.42	7.34	9.16	4.34	4.18
w/o Depth Error	9.90	7.55	6.09	11.13	5.86	5.51

Table 6. Ablation study of the pedestrian and cyclist categories on the KITTI val set.

Methods	Extra data	Test, IoU=0.5, $AP_{3D R40}$					
		Pedestrian			Cyclist		
		Easy	Mod.	Hard	Easy	Mod.	Hard
CaDDN [43]	LiDAR	12.87	8.14	6.76	7.00	3.41	3.30
OccupancyM3D [39]		14.68	9.15	7.80	7.37	3.56	2.84
MonoPGC [57]	Depth	14.16	<u>9.67</u>	<u>8.26</u>	5.88	3.30	<u>2.85</u>
GUPNet [33]	None	<u>14.72</u>	9.53	7.87	4.18	2.65	2.09
MonoCon [30]		13.10	8.41	6.94	2.80	1.92	1.55
DEVIANT [21]		13.43	8.65	7.69	5.05	3.13	2.59
MonoDDE [26]		11.13	7.32	6.67	5.94	3.78	3.33
MonoDETR [62]		12.65	7.19	6.72	5.12	2.74	2.02
MonoDGP (Ours)		None	15.04	9.89	8.38	5.28	2.82

Table 7. Comparisons of the pedestrian and cyclist categories on the KITTI test set. We **bold** the best results and underline the second-best results.

We also compare the pedestrian and cyclist detection results in Tab. 7. Specifically, our method achieves a superior performance on all levels of difficulty for pedestrian detection, benefiting from its simple and stable geometric structures. However, the performance for the cyclist category falls short of the best.

Notably, despite these geometric challenges, our cyclist detection performance remains competitive among methods without extra training data. This underscores the generalizability of RSH module for complex categories.

E. Sensitivity to Initial Features

Since error prediction mode heavily relies on good geometric features, the inaccuracies of initial features can significantly impact the convergence and performance of the proposed network. The Initial features, such as 3D dimension height (H_{3D}) and 2D bounding box height (h_{bbox}), are crucial for geometric depth calculation. To analyze their individual impacts, we conduct sensitivity experiments replacing predicted H_{3D} and h_{bbox} with ground truth values.

As shown in Tab. 8, the perfectly accurate geometric depth improves moderate AP_{3D} by up to 26.21%, highlighting the significance of these features. Compared to h_{bbox} , the network is more sensitive to H_{3D} errors due to its inherent difficulty as a 3D property. There also exists a coupling relationship between h_{bbox} and H_{3D} . Simultaneously replacing both features with ground truth values performs much better than replacing them individually. Current limitations mainly arise from height prediction error accumulation in the perspective projection. Improvements in monoc-

Geometric Depth ($f \times H_{3D}/h_{bbox}$)		Val, IoU=0.7, $AP_{3D R40}$		
Ground Truth H_{3D}	Ground Truth h_{bbox}	Easy	Mod.	Hard
✗	✗	30.76	22.34	19.01
✓	✗	39.10	31.89	27.51
✗	✓	33.62	25.04	21.97
✓	✓	57.81	48.55	41.92

Table 8. Sensitivity study on the KITTI val set for the car category.

Depth Prediction Mode	Val, IoU=0.7, $AP_{3D R40}$		
	Easy	Mod.	Hard
Direct Depth	24.33	18.87	15.31
DAv2-small (HS) + Depth Error	11.45	9.11	7.86
DAv2-small (VK2) + Depth Error	27.04	20.48	17.52
DAv2-base (VK2) + Depth Error	27.86	21.15	18.10

Table 9. Ablation Study of pre-trained MDE. ‘DAv2’ denotes Depth Anything V2 [61] method, ‘HS’ denotes pre-trained on indoor dataset Hypersim [44], ‘VK2’ denotes pre-trained on outdoor dataset Virtual KITTI 2 [6].

ular features, particularly for H_{3D} , will further enhance the performance of error prediction in the future.

F. Initial Depth from Pre-trained MDE

Monocular depth estimation (MDE) models have developed for many years. We can also utilize the pre-trained MDE to provide a roughly approximate surface depth, similar to geometric depth, which may render the learning problem even simpler.

To explore this possibility, we exploit Depth Anything V2 [61] to generate depth maps. Based on the initial metric depth, error prediction can achieve better performance compared to direct prediction in Tab. 6. However, MDE heavily relies on pre-trained datasets, while geometric depth relies on its own attributes without additional parameters. This will limit the generalization of achieving initial depth from pre-trained MDE.

G. Experiments on Waymo Open Dataset

Waymo [52] evaluates objects at Level_1 and Level_2, which are determined by the number of LiDAR points within their 3D bounding boxes. The experiments is conducted across three distance ranges: [0, 30), [30, 50), and [50, ∞) meters. Performance on the Waymo dataset is assessed by average precision AP_{3D} and average precision weighted by heading APH_{3D} .

We follow the DEVIANT [21] split to generate 52,386 training and 39,848 validation images by sampling every third frame. For fairness, we mainly compare with methods using the same split in Tab. 10. Our method achieves state-of-the-art performance without extra data across all ranges, particularly for distant objects. These results further validate the effectiveness and generalizability of MonoDGP. It

Difficulty	Methods	Extra	AP_{3D}				APH_{3D}			
			All	0-30	30-50	50- ∞	All	0-30	30-50	50- ∞
Level.1(IoU=0.7)	CaDDN [43]	LiDAR	5.03	15.54	1.47	0.10	4.99	14.43	1.45	0.10
	PatchNet [34] in [55]	Depth	0.39	1.67	0.13	0.03	0.39	1.63	0.12	0.03
	PCT [55]	Depth	0.89	3.18	0.27	0.07	0.88	3.15	0.27	0.07
	M3D-RPN [4] in [43]	None	0.35	1.12	0.18	0.02	0.34	1.10	0.18	0.02
	GUPNet [33] in [21]	None	2.28	6.15	0.81	0.03	2.27	6.11	0.80	0.03
	DEVIANT [21]	None	2.69	6.95	<u>0.99</u>	0.02	2.67	6.90	<u>0.98</u>	0.02
	MonoUNI [18]	None	<u>3.20</u>	<u>8.61</u>	0.87	<u>0.13</u>	<u>3.16</u>	<u>8.50</u>	<u>0.86</u>	<u>0.12</u>
	MonoDGP (Ours)	None	4.28	10.24	1.15	0.16	4.23	10.10	1.14	0.16
Level.2(IoU=0.7)	CaDDN [43]	LiDAR	4.49	14.50	1.42	0.09	4.45	14.38	1.41	0.09
	PatchNet [34] in [55]	Depth	0.38	1.67	0.13	0.03	0.36	1.63	0.11	0.03
	PCT [55]	Depth	0.66	3.18	0.27	0.07	0.66	3.15	0.26	0.07
	M3D-RPN [4] in [43]	None	0.35	1.12	0.18	0.02	0.33	1.10	0.17	0.02
	GUPNet [33] in [21]	None	2.14	6.13	0.78	0.02	2.12	6.08	0.77	0.02
	DEVIANT [21]	None	2.52	6.93	<u>0.95</u>	0.02	2.50	6.87	<u>0.94</u>	0.02
	MonoUNI [18]	None	<u>3.04</u>	<u>8.59</u>	<u>0.85</u>	<u>0.12</u>	<u>3.00</u>	<u>8.48</u>	<u>0.84</u>	<u>0.12</u>
	MonoDGP (Ours)	None	4.00	10.20	1.13	0.15	3.96	10.08	1.12	0.15
Level.1(IoU=0.5)	CaDDN [43]	LiDAR	17.54	45.00	9.24	0.64	17.31	44.46	9.11	0.62
	PatchNet [34] in [55]	Depth	2.92	10.03	1.09	0.23	2.74	9.75	0.96	0.18
	PCT [55]	Depth	4.20	14.70	1.78	0.39	4.15	14.54	1.75	0.39
	M3D-RPN [4] in [43]	None	3.79	11.14	2.16	0.26	3.63	10.70	2.09	0.21
	GUPNet [33] in [21]	None	10.02	24.78	4.84	0.22	9.94	24.59	4.78	0.22
	DEVIANT [21]	None	10.98	26.85	5.13	0.18	<u>10.89</u>	<u>26.64</u>	<u>5.08</u>	0.18
	MonoUNI [18]	None	<u>10.98</u>	<u>26.63</u>	4.04	0.57	<u>10.73</u>	<u>26.30</u>	<u>3.98</u>	<u>0.55</u>
	MonoDGP (Ours)	None	12.36	31.12	5.78	1.24	12.18	30.68	5.71	1.22
Level.2(IoU=0.5)	CaDDN [43]	LiDAR	16.51	44.87	8.99	0.58	16.28	44.33	8.86	0.55
	PatchNet [34] in [55]	Depth	2.42	10.01	1.07	0.22	2.28	9.73	0.97	0.16
	PCT [55]	Depth	4.03	14.67	1.74	0.36	4.15	14.51	1.71	0.35
	M3D-RPN [4] in [43]	None	3.61	11.12	2.12	0.24	3.46	10.67	2.04	0.20
	GUPNet [33] in [21]	None	9.39	24.69	4.67	0.19	9.31	24.50	4.62	0.19
	DEVIANT [21]	None	10.29	<u>26.75</u>	<u>4.95</u>	0.16	10.20	<u>26.54</u>	<u>4.90</u>	0.16
	MonoUNI [18]	None	<u>10.38</u>	<u>26.57</u>	3.95	0.53	<u>10.24</u>	<u>26.24</u>	<u>3.89</u>	<u>0.51</u>
	MonoDGP (Ours)	None	11.71	31.02	5.61	1.17	11.56	30.58	5.54	1.15

Table 10. Results on the Waymo val set for the vehicle category. Compared with methods without extra data, we **bold** the best results and underline the second-best results.

is worth noting that CaDDN [43]’s performance is better than MonoDGP, this discrepancy may be attributed to different dataset splits and introduction of LiDAR data.

further improvements in handling height occlusion, potentially through the integration of additional contextual information or more robust occlusion-aware models.

H. Qualitative Discussion and Visualization

To provide a more intuitive comparison between our method and the baseline models, we visualize some 3D detection results from both the camera view and the bird’s-eye view on the KITTI validation set. As shown in Fig. 10, our method demonstrates superior performance on distant and length-occluded objects.

However, since error prediction is affected by the initial accuracy of geometric depth, which is calculated from height relationships, height occlusion remains a challenge for our method. For the leftmost vehicle in the third example of Fig. 10, bushes block out its lower part, weakening the accuracy of height and consequently propagating errors to depth prediction. This failure case highlights the need for



(a) MonoCD

(b) MonoDETR

(c) MonoDGP(Ours)

Figure 10. Qualitative results on KITTI validation set. (a) MonoCD (b) MonoDETR (c) MonoDGP (ours). In each group of images, the first row shows the camera view, and the second row shows the bird’s-eye view. **Green** represents the ground truth of boxes, while **Red** represents the prediction results. We also circle some objects to highlight the difference between the baseline model and our method.